Water Resources Research

RESEARCH ARTICLE
10.1029/2024WR038923

Experimental Study on Hysteresis During Cyclic Injection in Hierarchical Porous Media

Shuo Yang[1], **Si Suo**[2], **Yixiang Gan**[3], **Shervin Bagheri**[2], **Lei Wang**[1], **and Johan Revstedt**[1]

[1]Department of Energy Sciences, Lund University, Lund, Sweden, [2]FLOW, Department of Engineering Mechanics, KTH Royal Institute of Technology, Stockholm, Sweden, [3]School of Civil Engineering, The University of Sydney, Sydney, NSW, Australia

Key Points:

- The differences in invasion dynamics during gas-liquid cyclic injection between hierarchical and uniform porous structures were studied
- The hysteresis effect was quantified by the Land model, revealing a weaker saturation hysteresis effect in the hierarchical structure
- The discrepancy in the relationship between relative permeability and saturation was investigated based on the van Genuchten model

Supporting Information:

Supporting Information may be found in the online version of this article.

Correspondence to:

S. Yang,
shuo.yang@energy.lth.se;
yangshawn65@gmail.com

Citation:

Yang, S., Suo, S., Gan, Y., Bagheri, S., Wang, L., & Revstedt, J. (2025). Experimental study on hysteresis during cyclic injection in hierarchical porous media. *Water Resources Research*, *61*, e2024WR038923. https://doi.org/10.1029/2024WR038923

Received 28 NOV 2024
Accepted 5 FEB 2025

Author Contributions:

Conceptualization: Shuo Yang, Si Suo, Yixiang Gan, Shervin Bagheri, Lei Wang, Johan Revstedt
Data curation: Shuo Yang
Formal analysis: Shuo Yang, Si Suo, Yixiang Gan, Shervin Bagheri
Investigation: Shuo Yang
Methodology: Shuo Yang, Si Suo, Yixiang Gan, Shervin Bagheri, Lei Wang, Johan Revstedt
Project administration: Johan Revstedt
Resources: Shervin Bagheri
Software: Shuo Yang, Si Suo
Supervision: Shervin Bagheri, Lei Wang, Johan Revstedt
Validation: Shuo Yang

Abstract Cycle injection schemes are often encountered in underground hydrogen storage (UHS), and the involved hysteresis directly impacts storage and extraction efficiency. The geological formation generally has hierarchical features containing multiple-level pore sizes. Nevertheless, we still lack a comprehensive understanding of this phenomenon and the pore-scale mechanism behind the geometry affects saturation hysteresis and its cyclic responses. In this work, by 3D printing technology, we fabricated a hierarchically structured porous media with dual permeability and uniform one for comparison. Gas-liquid injection cycles were performed to investigate the impact of hierarchical structure on invasion behavior. The phase morphology shows the preferential invasion in 1st-order structure and the capillary trapping in 2nd-order structure, which are supported by the phase saturation at each level of the hierarchical structure. Furthermore, ganglion motion is suppressed in the hierarchical structure. Through analyzing local invasion behaviors, the connect-jump invasion mode is identified as the primary reason for this suppression. Then, the hysteresis effect was quantified based on the Land model, revealing a weaker hysteresis effect in the hierarchical structure compared with the uniform structure, indicating that the hierarchical structure has a lower storage and extraction efficiency in UHS. Finally, the upward trend of relative permeability with saturation was fitted by the van Genuchten model. The model parameter in the hierarchical structure is higher than that in the uniform structure, which is caused by extra pore space in 2nd-order structure. The findings improve the understanding of hysteresis effect and can promote optimizing strategies for storage and extraction in UHS.

Plain Language Summary Understanding how hydrogen and underground liquid move through porous materials with varied pore sizes is crucial for improving the strategy of underground hydrogen storage (UHS), a promising solution for green energy needs. In this work, we fabricated a hierarchical porous structure with multiple pore sizes to mimic the natural geological rock formation. Our research focused on how this hierarchical structure influences fluid behavior during gas and liquid injections. The results reveal significant differences in fluid flow behavior across different levels of the hierarchical structure. Quantitative discrepancies in gas saturation, permeability, and connectivity were also observed between hierarchical and uniform structures. For example, the hierarchical structure has higher connectivity and permeability due to the additional pore space provided by its 2nd-order pores. Furthermore, the hierarchical structure demonstrates a weaker hysteresis effect-a phenomenon where past fluid movements impact current behavior. This weaker hysteresis effect suggests that the hierarchical structure in the rock formation reduces the storage and extraction efficiency in UHS application. These findings provide the references for the selection of hydrogen storage sites and insights into optimizing the strategies for underground resource applications.

1. Introduction

Immiscible fluid-fluid displacement in porous media has attracted increasing attention due to its wide applications in subsurface extraction/storage, that is, underground hydrogen storage (UHS) (Broers et al., 2021), geological carbon sequestration (Bakhshian & Sahimi, 2017; Celia et al., 2015), underground water contamination (Das & Nassehi, 2003), and remediation of nonaqueous liquids (Porter et al., 2010). Today, hydrogen energy (D. Yang et al., 2024) is being developed as a promising green energy in response to growing energy demand and the urgent need to mitigate climate change. Underground hydrogen storage (UHS) in depleted hydrocarbon fields and aquifers holds great promise (Hematpur et al., 2023; Tarkowski, 2019). However, UHS technology is still in the early development stage, and pressing challenges remain that hinder its wider and rapid adaptation, including

Visualization: Shuo Yang
Writing – original draft: Shuo Yang
Writing – review & editing: Shuo Yang, Si Suo, Yixiang Gan, Shervin Bagheri, Lei Wang, Johan Revstedt

hydrogen loss during cyclic operation and lack of accurate assessment and optimization tools for storage (Zhong et al., 2024).

UHS includes temporary storage and later-on extraction (use) processes, corresponding to the cyclic displacement of H_2 injection (drainage) and withdrawal (waterflooding) (Lysyy et al., 2023). In UHS, a certain quantity of hydrogen (H_2) lost may be irreversible due to residual trapping. Throughout the cyclic injection process, the trapped H_2 might reconnect owing to the hysteresis of saturation (Wang et al., 2023) and relative permeability (Lysyy et al., 2022). Over the past few decades, numerous models to describe gas trapping have been developed. The widely used trapping models, including the Land model (Land, 1968), Carlson model (Carlson, 1981), and Jerauld model (Jerauld, 1997), define ultimate residual saturation as a function of the initial water saturation. Wang et al. (2023) employed an interface tracking algorithm to simulate displacement processes during cycle injection, analyzed the evolution of saturation hysteresis with each injection cycle, and compared the initial and residual CO_2 saturation. The findings indicate that the system approached to hysteresis equilibrium as the injection cycles progressed. However, contrary to the predictions of the classic Land trapping theory (Land, 1968), the total residual saturation increase over successive injection cycles. This trend has been observed in other studies as well (Edlmann et al., 2019; Herring et al., 2021; Lysyy et al., 2023). Explanation of this inconsistency between the model prediction and result requires more in-depth research on the mechanism of saturation hysteresis.

Recent research efforts have primarily concentrated on heterogeneous porous media, encompassing surface attributes such as wettability (Hu et al., 2019; Wang et al., 2019), as well as topological features, such as pore size distribution (Lu et al., 2019; Rabbani et al., 2018), variable depth (Lei et al., 2023, 2024), and connectivity (Herring et al., 2013; S. Yang et al., 2024). In the literature, the research on geometry impacts is divided into two types of heterogeneous porous media: random and patterned structures. For a random porous medium, Wang et al. (2019) demonstrated that as the structural disorder decreases, the interface tends to stabilize. Previous studies have also explored the intricate relationship between wettability and disorder (Hu et al., 2019; Wang et al., 2019). For a patterned porous medium, manipulating the pore size gradient along the flow direction has emerged as an effective strategy for mitigating viscous fingering (Rabbani et al., 2018) and capillary fingering (Lu et al., 2019). However, these studies only considered the porous structures with one level of pore sizes. In natural subsurface rock formations and synthetic materials, such as porous electrodes and fibrous materials, porous structures typically exhibit multiple levels of pore sizes. Previous studies have revealed that sharp stratification (Datta & Weitz, 2013; Nijjer et al., 2019), dual permeability (Liu et al., 2014; Zhang et al., 2011), and dual porosity (Gu et al., 2021; Kang & Wang, 2024; Lei et al., 2024; Wolf et al., 2022) within the porous structure can significantly alter fluid pathways. These dual structures directly divide into upper and lower layers. In practical applications, apart from the evident layering, various levels of pore sizes are typically distributed across the entire porous domain. This configuration constitutes a hierarchical or fractal structure characterized by dual permeability. Suo et al. (2020) first investigated numerically viscous fingering (Suo et al., 2020) and capillary fingering (Suo & Gan, 2021) in hierarchically structured porous media and discovered three fluid-fluid displacement modes. By considering two key factors, that is, driving pressures and interaction durations, a dimensionless hierarchical number was proposed to characterize the effect of hierarchical structure on displacement behavior. These contrasting characteristic length scales (Suo et al., 2020) pose significant challenges to the experimental research on gas-liquid flow, in terms of both the fabrication and observation of samples. Therefore, experimental research on gas-liquid cyclic injection in such hierarchical porous structure has not been reported in the literature, resulting in the lack of understanding of the geometrical effects on the pore-scale, especially for viscous-dependent immiscible displacement.

To comprehensively investigate the impacts of geometry on cyclic gas-liquid displacements in porous media, in this work, we employ two designs for microfluidic experiments, that is, a designed hierarchical porous structure and the corresponding uniform one for comparison. The 3D printing technique is employed to fabricate these two types of micromodels. Employing N_2-water cyclic injection, displacement morphologies are visualized at each steady state by a microfluidic imaging platform. We explore the impact of hierarchical structure and invasion flow rate by analyzing saturation evolution. To characterize the hysteresis effects, the Land model is employed as a reference framework. The mobilization of residual ganglion and local invasion behavior are analyzed to explore the underlying mechanism. The cause of the difference in saturation hysteresis between uniform and hierarchical structures is further revealed from the perspective of topological connectivity and fluid conductivity, that is, normalized Euler number and relative permeability, respectively.

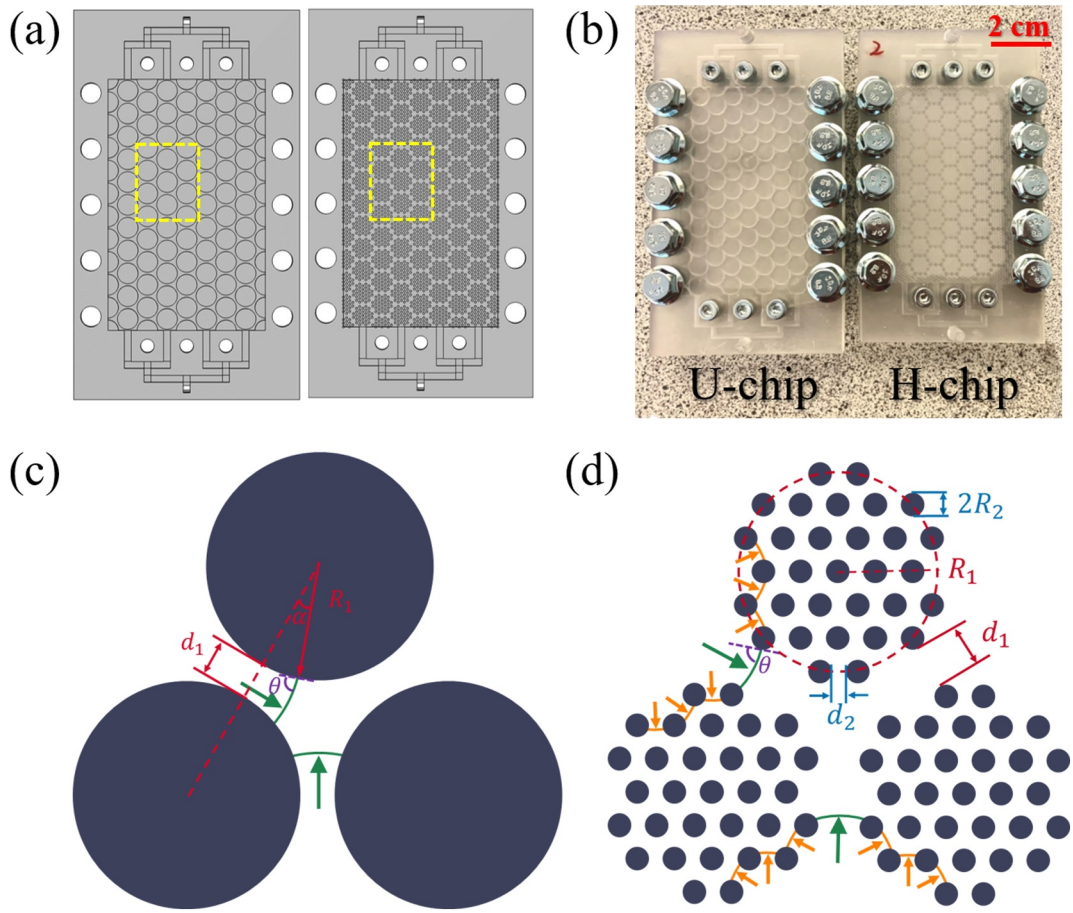

Figure 1. Geometries of the uniform and hierarchical porous media model. (a) The schematic diagrams. (b) 3D printed uniform and hierarchical models, named *U-model* and *H-model*, respectively. The periodic geometries of (c) the uniform model with 1st-order structure and (d) the hierarchical model with 1st-order and 2nd-order structures.

2. Materials and Methods

As shown in Figure 1a, 2D microfluidic porous media model was used in this study. This porous media model consists of upper and lower plates, which were printed separately using resin materials by a 3D printer (Formlabs Form 3+, with a spatial resolution of 200 μm). The upper plate is just a flat plate, while the lower plate contains the porous domain and the inlet and outlet channels. As illustrated in Figure 1b, the lower and upper plates were fixed by screws on the margin of the model. The porous domain has two different designs adopted in this study, that is, a uniform (*U-model*) and a hierarchical (*H-model*) porous media. *U-model* has a periodic structure, as shown in Figure 1c, whose periodic cell is designed as a regular hexagonal arrangement controlled by the cylinder radius R_1 and neighboring gap size d_1. *H-model* is a dual-permeability medium, containing 1st-order and 2nd-order porous structures. The arrangement of the 1st-order structure is the same with the uniform design, and each solid cylinder is composed of the 2nd-order structure arranged in a self-similar manner, whose periodic cell is controlled by R_2 and d_2, as shown in Figure 1d. The porous domains in *U-model* and *H-model* are both $69.96 \times 44.06 \times 1.00$ mm and other geometric details including characteristic sizes and porosity φ of both designs are summarized in Table 1. Porosity φ in each order structure was calculated by the pore space area divided by total porous domain area in each order structure. The detailed calculation of φ_{1st} and φ_{2nd} can be found in Figure S3 in Supporting Information S1. The minimum pore features, R_2 and d_2, were selected to guarantee that the printer resolution is sufficient to represent the desired structures.

For directly observing cyclic gas-liquid displacements in porous media under various flow rates, we set up an experimental platform, as illustrated in Figure 2, including an injection control system, a micromodel, and a data collection system. We used N_2 as an analogous gas in this study. Although the density and viscosity of H_2 are

Table 1
Geometric Parameters of the Two Microfluidic Model Designs

	1st-order structure			2nd-order structure		
	d_1 (mm)	R_1 (mm)	φ_{1st} (%)	d_2 (mm)	R_2 (mm)	φ_{2nd} (%)
H-model	0.66	3.00	19.24	0.42	0.30	62.17
U-model	0.66	3.00	17.40	/	/	/

lower than that of N_2, the difference is negligible compared to water. In addition, a recent study by Rezaei et al. (2022) demonstrated that H_2 and N_2 exhibit very similar relative permeability profiles during unsteady state drainage, suggesting that N_2 can be used as a substitute for H_2 in flow experiments, thereby reducing health and safety risks. Therefore, we finally decided to use N_2-water system in this study. Initially, the micromodel was filled with N_2 and then deionized water was first injected to displace N_2 at a given flow rate (30, 85, and 170 mL/hr) controlled by the syringe pump (New Era NE-4000) until the waterflooding reached a steady state. Steady state was determined when the invasion area reached the maximum and the invading pattern no longer changed (S. Yang et al., 2022). Afterward, N_2 was injected to drain the water at the same flow rate as waterflooding controlled by a mass flow meter (Bronkhorst EL-Flow prestige FG-200CV) until another steady state was reached. Such waterflooding-drainage process would be repeated. We found that after repeating 4 times, the saturation of each invading phase remained unchanged each time, which is called hysteresis equilibrium. Therefore, in this work, we only took the results of the 4 cycles, which were named L0 → G1 → L1 → G2 → L2 → G3 → L3 → G4 → L4 ("L" represents liquid invasion and "G" represents gas invasion). The dynamics of gas-liquid cyclic displacement was captured by a high-speed camera (Phantom V611 camera with a lens of micro-NIKKOR 105 mm) with 25 ~ 50 fps and 30 μs exposure time, and the size of the porous domain of interest was 1,280 × 800 in pixel with the spatial resolution of 61.5 μm/pixel. An advanced image processing technique, as detailed in Figure S5 in Supporting Information S1 and our previous works (S. Yang et al., 2021, 2022), was employed to identify and extract gas, liquid, and solid phases, respectively. To differentiate between the phases, blue, red, and gray represent the liquid, gas, and solid phases, respectively. Light red and light blue marked the area newly occupied by gas and liquid, respectively, representing active areas during the invasion. The newly invaded area is obtained by taking a difference between the invasion pattern captured in the previous and current invasion processes. Digital image processing was also used to calculate saturation and Euler number. The physical properties of deionized water and N_2 at the lab conditions (~22°C) are shown in Table 2. The density, viscosity and surface tension of deionized water are sourced from the studies by Tanaka et al. (2001), Korson et al. (1969), and

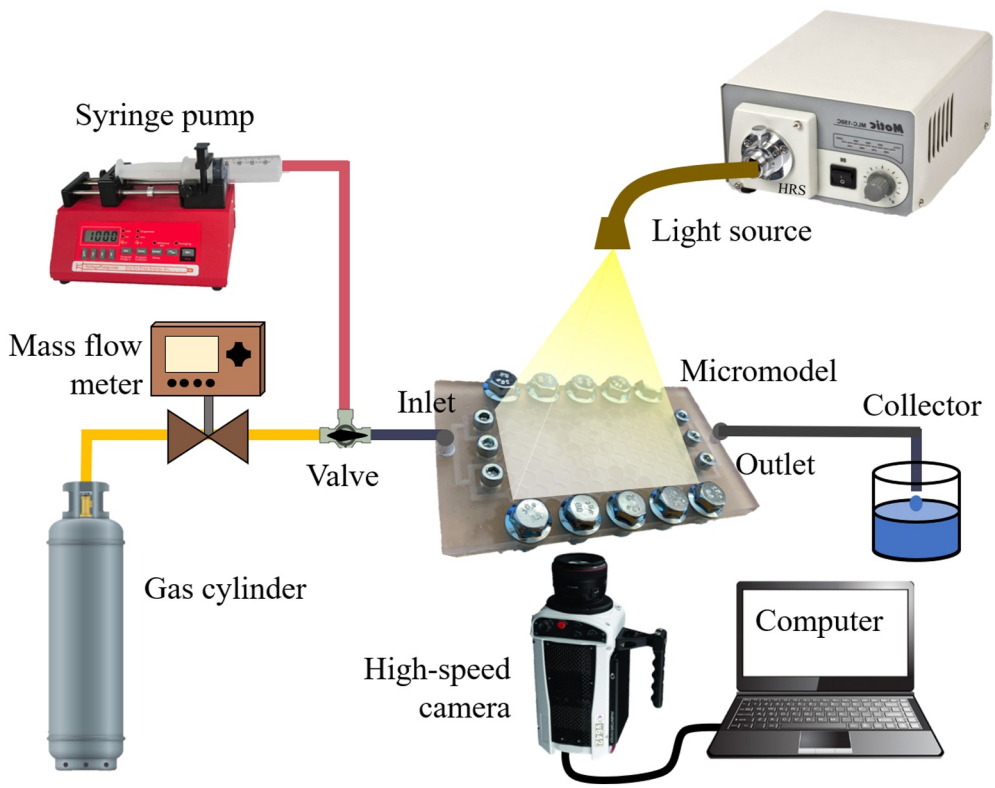

Figure 2. Schematic diagram of experimental setup for cyclic gas-liquid displacements.

Table 2
Physical Properties of Fluids at the Lab Conditions (~22°C)

	Deionized water	N_2
Density, ρ (kg/m^3)	998.2	1.138
Viscosity, μ (mPa s)	1.01	0.0179
Surface tension, γ (N/m)	0.0728	/
Contact angle, θ	75 ° ± 2°	/

Vargaftik et al. (1983), respectively. The density and viscosity of N_2 are based on the measurements provided by Seibt et al. (2006). The contact angle of water on the resin material is 75 ° ± 2° measured by Drop Shape Analyzer (DSA25S SN 30016603). Therefore, the 2D microfluidic porous media model fabricated in this study is weakly hydrophilic. During waterflooding process, the corresponding capillary number $Ca = \frac{\mu_L U_L}{\gamma}$ varies from 2.57×10^{-6} to 1.46×10^{-5} with the viscosity ratio (liquid to gas) M_{LG} equal to 56.4. During drainage process, capillary number $Ca = \frac{\mu_G U_G}{\gamma}$ varies from 4.55×10^{-8} to 2.58×10^{-7} with the viscosity ratio (gas to liquid) M_{GL} equal to 0.0177. Here, μ_L and μ_G are the viscosity of liquid and gas, and U_L and U_G are the Darcy velocity of liquid and gas, respectively. γ is the surface tension. Therefore, all the cases are both located in the capillary fingering regime, suggesting that cyclic invasion is capillary-dominated. To validate the reproducibility of the experimental platform, the most unstable case was chosen to repeat the experiment, that is, the hierarchical chip with the highest injected flow rate 170 mL/hr. The results qualitatively and quantitatively validate the reproducibility of the experimental platform. A detailed description is given in the Text S1 in Supporting Information S1.

3. Results and Discussion

3.1. Effect of Geometry and Invasion Flow Rate

We begin by qualitatively comparing the fluid displacement patterns at steady state of each cycle between uniform and hierarchical structures. Taking 170 mL/hr as an example in Figures 3a and 3b, in cycle 0, we injected liquid to displace the gas that originally occupied the pore space. Since liquid viscosity is much larger than that of the gas and solid surface is weakly wettable, the displacement is favorable and the gas-liquid interface maintains

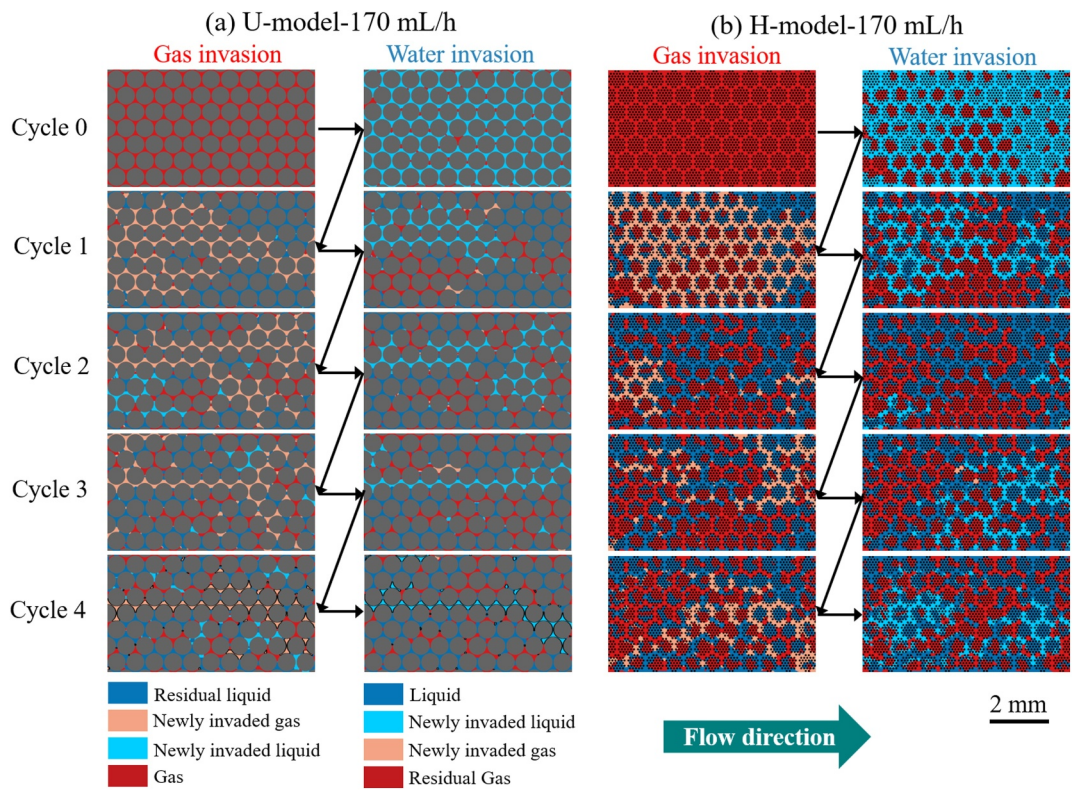

Figure 3. Comparison of displacement patterns at steady state of each cycle between uniform and hierarchical structures. (Blue and red represent the liquid and gas phases, respectively. The light blue and light red represent the newly invaded liquid and gas, respectively. The numbers above the figure represent the injection flow rate. The results at the injection flow rate of 30 and 85 mL/hr can be found in Figure S6 in Supporting Information S1).

stable during the waterflooding process. In *U-model* liquid displaced most of the gas phase, only leaving a few tiny gas ganglia distributed along the streamwise direction. However, in *H-model*, a large number of gas clumps were left in the 2nd-order pore space though the 1st-order pore space was clearly displaced by the liquid. After the first waterflooding process, the first drainage process followed as shown in gas invasion in cycle 1 of Figure 3a. Due to the low viscous ratio, the interface becomes unstable and a finger pattern occurs in *U-model*, leaving a large portion of uninvaded areas. In *H-model*, the gas invasion pattern of cycle 1 shows that gas prefers to invade 1st-order structure during the first drainage process.

Apart from the structure effect, injection flow rate also plays a very important role in the waterflooding and drainage process. In UHS application, alteration in Darcy velocity impacts pressure balance and invasion speed in porous media, consequently affecting sweep efficiency (storage and extraction efficiency). Additionally, the flow rate of injection is crucial for selecting appropriate pumping equipment, further influencing economic cost (S. Yang et al., 2022). Therefore, the influence of injection flow rate was investigated in this study. The results at the injection flow rate of 30 and 85 mL/hr can be found in Figure S6 in Supporting Information S1. It was shown that the same preceding phenomena of the preferential invasion in 1st-order structure and stronger capillary trapping in 2nd-order structure persist for all injection flow rates. After the first water invasion at a low flow rate of 30 mL/hr in *U-model* (Figure S6e in Supporting Information S1), uninvaded areas can be observed at the corners of the porous domain on the outlet side, which disappears at higher flow rates. As the number of cycles injection in *U-model* increases, both gas and liquid invasions gradually stabilize into the same path as shown in light color with the black edge in Figure S6a in Supporting Information S1. The invading fluid invades mainly in the forward direction and the thin and straight invaded paths are observed in light colors in *U-model* cycle 4 of Figures S6a, S6c, and S6e in Supporting Information S1. At a lower flow rate (Figure S6e in Supporting Information S1), the invaded path exhibits more tortuous in cycle 4 of *U-model*. In the 2nd-order structure of *H-model* (Figures S6b, S6d, and S6f in Supporting Information S1), the displacement pattern after the water invasion of cycle 0 remains almost constant, which indicates that gas remains trapped. In the 1st-order structure of *H-model*, the invading phase always invades in a similar position and the invasion pattern can stabilize into the same path at the lower invasion flow rates (Figures S6d and S6f in Supporting Information S1)) but not at the highest invasion flow rates during cyclic injection (Figure S6b in Supporting Information S1). In addition to qualitative comparisons, we performed quantitative analyses. The saturation of the newly invaded area (light-colored regions in Figure S6 in Supporting Information S1) was calculated during cyclic gas-liquid injections. Further details are provided in Text S8 in Supporting Information S1. As shown in Figure S9 in Supporting Information S1, the newly invaded phase saturation $S_{ip,new}$ in both the *H-model* and *U-model* decreases rapidly as the cycle number increases. After the third gas injection, $S_{ip,new}$ in the *U-model* gradually stabilizes, whereas in the *H-model*, it shows a slight upward trend. Overall, both qualitative and quantitative analyses indicate that the displacement pattern in uniform structure stabilizes more easily during cyclic invasion.

In *H-model*, the smaller newly invaded area is observed at the lower invasion speeds (Figures S6d and S6f in Supporting Information S1) due to lower driving pressure difference. The gas distribution is relatively dispersed at the flow rate of 170 mL/hr (Figure S6b in Supporting Information S1). At lower flow rates (Figures S6d and S6f in Supporting Information S1), a large cluster of gas was generated in the hierarchical structure, which is difficult to mobilize in subsequent cycles. The gathered distribution of the gas phase allows the displacement pattern to stabilize at an earlier number of cycles. The two necessary conditions for the formation of large gas clusters are related to entry capillary pressure and driving force. The driving force must be large enough to overcome the entry capillary pressure to destroy the gas clusters. The driving force stems from the pressure difference, which is positively correlated with the injection flow rate. Therefore, such gas clusters only appear at lower flow rates as shown in displacement patterns of *H-model* in Figure S6 in Supporting Information S1. At low flow rates, the liquid cannot easily penetrate the large gas clusters and instead follows existing liquid channels to breakthrough (e.g., the blue area near the upper boundary in Figures S6d and S6f in Supporting Information S1). More details about entry capillary pressure will be discussed in Section 3.3.

Apart from the qualitative comparison between uniform and hierarchical structures above, it is also worthwhile to conduct quantitative comparisons, that is, saturation, topology connectivity, and permeability. By using an image processing procedure (S. Yang et al., 2021, 2022), the invaded area of invading phase during each cycle was measured. Then the saturation of invading phase can be calculated as:

10.1029/2024WR038923

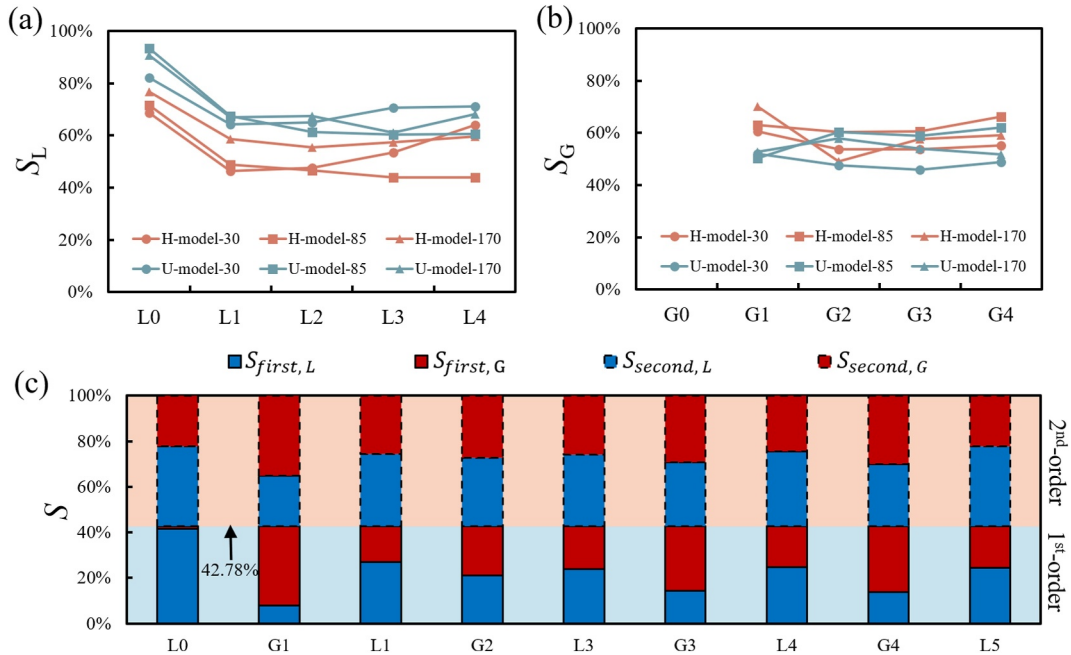

Figure 4. Saturation of (a) liquid phase and (b) gas phase during cyclic liquid and gas invasion in uniform and hierarchical structures, (c) liquid and gas saturation in various order structure of hierarchical model at 170 mL/hr flow rate. (Solid border: 1st-order structure and dotted border: 2nd-order structure. 42.78% is the proportion of pore space in 1st-order structure).

$$S = \frac{A}{L_{\text{total}}\, W_{\text{total}}\, \varphi} \tag{1}$$

Here, A is the invaded area of invading phase, L_{total} and W_{total} are the length and width of the porous domain. φ is the total porosity of porous domain. The results are separated into liquid invasion (Figure 4a) and gas invasion (Figure 4b). Figure 4a illustrates the declining trend in S_L for both *U-model* and *H-model* as the number of cycles increases. The curves gradually become flat during the cyclic invasion of both *U-model* and *H-model*, both fluctuating within the range from 50% to 70%. As shown in Figure 4a, the liquid saturation S_L of the *U-model* is higher than that of *H-model* during liquid cyclic invasion. The strong gas trapping effect in 2nd-order structure of *H-model* mentioned above leads to a large amount of residual gas. As shown in Figure 4b, there is no significant difference in S_G for *U-model* and *H-model* during gas cyclic invasion. Note that the intrinsic porous spaces available in both structures are different, and *H-model* contains the additional 2nd-order structures contributing to the overall cyclic saturation behavior. The stacked column charts of saturation in 1st-order structure (lower two columns with solid borders) and 2nd-order structure (the upper two columns with dotted borders) in Figure 4c illustrate the evolution of saturation during the cyclic invasion process in the different orders of hierarchical structures. Figure 4c indicates that the changes in gas and liquid saturations within the 1st-order structure are more significant than those in the 2nd-order structure during cyclic invasion. This result is consistent across all injection flow rates, as detailed in Figure S7 in Supporting Information S1. It reconfirms the earlier findings regarding the preferential invasion in 1st-order structure and strong capillary trapping of 2nd-order structure.

The declining trend of S_L in Figure 4a is a manifestation of the saturation hysteresis effect during cyclic injection. The hysteresis effect refers to a phenomenon where a system's state depends not only on its current conditions but also on its history. This lag or memory effect causes the system to respond differently when conditions are increasing and decreasing. In porous media undergoing cycles of gas saturation (drainage) and desaturation (imbibition), the capillary pressure–saturation curve during imbibition does not retrace the same path as during drainage, creating a hysteresis loop. In addition to fluid trapping and contact angle hysteresis, pore geometry effects greatly influence the hysteresis effect. Understanding and accounting for hysteresis are crucial for accurately modeling and optimizing processes like UHS, as it affects saturation levels and the efficiency of gas

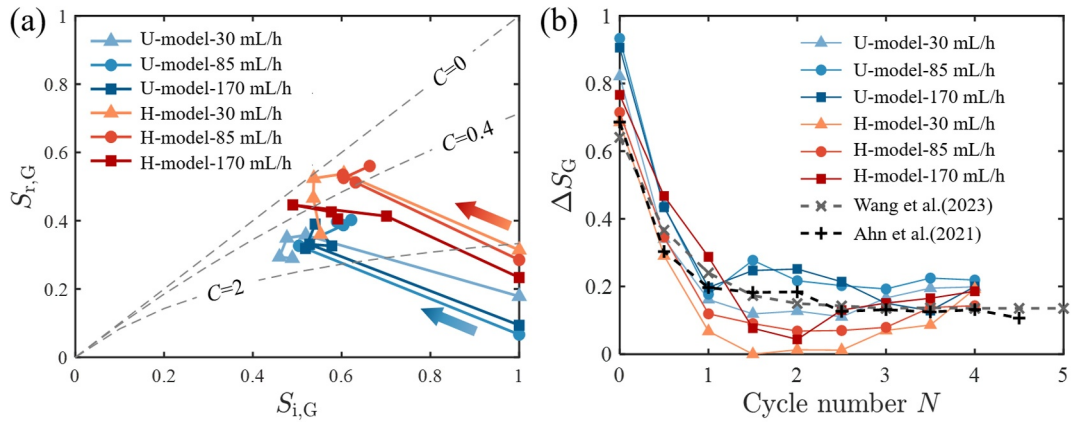

Figure 5. (a) Trajectories of initial and residual gas saturation during cyclic injections with varying invasion flow rates in uniform and hierarchical structures (Two gray dashed curves and one diagonal dashed line are plotted when Land trapping coefficient C is equal to 0.4, 2, and 0.), (b) evolution of gas saturation hysteresis ΔS_G with cycle number N in uniform and hierarchical structures (Dashed line with marker "+" and "×" are the experimental data (Ahn et al., 2020) and numerical data (Wang et al., 2023), respectively).

storage and extraction. In the next section, we will analyze the hysteresis effect and compare the difference between uniform and hierarchical structures in detail.

3.2. Hysteresis Effect of Cyclic Injection

We quantify the hysteresis effect during cyclic injection by using the Land trapping model (Land, 1968; Spiteri et al., 2008):

$$S_{r,G} = \frac{S_{i,G}}{1 + C\, S_{i,G}} \tag{2}$$

Here, the initial gas saturation $S_{i,G}$ and the residual gas saturation $S_{r,G}$ were obtained when the gas and liquid invasions reach steady state, respectively. Figure 5a illustrates the trajectories of $S_{i,G}$ and $S_{r,G}$ beginning from $S_{i,G} = 1$ during cyclic injections. These trajectories represent the evolution of saturation hysteresis throughout the cyclic injections. C is the Land trapping coefficient. Two gray dashed curves are plotted when C is equal to 0.4 and 2. In *U-model*, trajectories after cycle 0 both remain within the range of these two Gray dashed curves. In *H-model*, the residual gas saturation $S_{r,G}$ is higher than that in *U-model* due to the stronger capillary trapping effect of 2nd-order structure. Further, it can be noted that for all the injection flow rates the trajectories of *H-model* both exceed the upper boundary curve of 0.4. Subsequently, trajectories revert back toward higher C values. As the number of cyclic injections increases, the trajectories of *U-model* and *H-model* gradually stabilize within a small range, which indicates the hysteresis equilibrium. In order to clearly explain the different hysteresis phenomena, the hysteresis schematic diagrams for the different situations are shown in Figure 6. When hysteresis becomes equilibrium as shown in Figure 6a, the difference ΔS_G between $S_{r,G}$ and $S_{i,G}$ in the neighboring cycles will

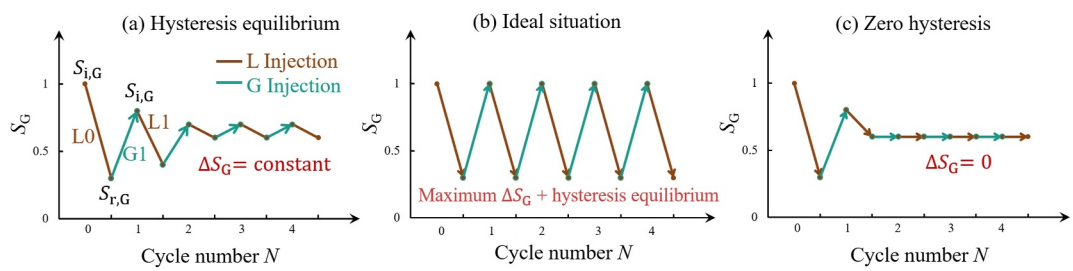

Figure 6. Hysteresis schematic diagrams for (a) hysteresis equilibrium, (b) ideal situation in underground hydrogen storage, and (c) zero hysteresis.

become constant as the increase of cycle number N. The stabilization of displacement pattern mentioned above is also the manifestation of hysteresis equilibrium. The trajectories of *H-model* move over a larger range than *U-model*, which means that it is more difficult for the hierarchical structure to reach hysteresis equilibrium.

In underground storage applications, ΔS_G is the amount of hydrogen that can be produced after storage and the amount that can be stored again after production. It is a crucial indicator for assessing the efficiency of storage and extraction processes. Ideally, as illustrated in Figure 6b, optimal efficiency is achieved when ΔS_G reaches and maintains the maximum capacity permitted by the storage site's porous structure, thereby sustaining hysteresis equilibrium. However, it is difficult to maintain a high level of ΔS_G in practice. Therefore, in order to quantify the level of hysteresis effect and assess the efficiency of storage and extraction processes in the hierarchical structure, ΔS_G at each cycle was calculated. Figure 5b shows how ΔS_G of *U-model* and *H-model* develops during the cyclic invasion at different flow rates. The results are compared with experimental and numerical data from the literature. The ΔS_G in literature was also collected during the capillary-dominated cyclic invasion with a slow invasion flow rate, which is consistent with the condition in our study. Wang et al. (2023) varied the contact angle in the range of 45°–135°, but we specifically compared the numerical data with a 90° contact angle due to its proximity to the contact angle of our cases. As shown in Figure 5b, the ΔS_G of our data initially experiences an exponential decay as the increase of cycle number N, closely aligning with the curves in literature (Ahn et al., 2020; Wang et al., 2023). Subsequently, ΔS_G curves of *H-model* reach the lowest points in cycle 2. These lowest points correspond to the point of trajectories that are close to the diagonal dashed line in Figure 5a, indicating zero hysteresis (C is equal to 0). As illustrated in the schematic diagram for zero hysteresis in Figure 6c, ΔS_G approaches zero during alternating gas and liquid invasion. This indicates that the gas and liquid saturations in the porous medium remain constant with each injection cycle. Because no new area is invaded, this case corresponds to zero efficiency of the storage and extraction processes in the UHS, indicating the rock formation represented by this porous medium is unsuitable for UHS. Comparatively, as shown in Figure 5b, the ΔS_G evolution of *U-model* lies above that of *H-model*, indicating that the hierarchical structure has a weaker saturation hysteresis effect and lower efficiency of storage and extraction processes. This difference in hysteresis prompts us to further investigate the mechanism behind it.

3.3. Local Invasion Behavior and Residual Ganglion Motion

Before starting to discuss residual ganglia motion, we first revisit the discrete-domain model by Cueto-Felgueroso and Juanes (2016), which can be used to explain the difference in pore filling events between uniform and hierarchical structures during cycle injection. In this model, porous media is considered as an interconnected capillary tube network with multiple stable configurations. The diameter of these capillary tubes varies non-monotonically along the axial position. Macroscopical invasion behavior observed in the porous media stems from the collective behavior of these capillary tubes. Consequently, the invasion path and menisci movement are influenced by the local energy barrier of the capillary tube, that is, entry capillary pressure. Figures 1c and 1d show the meniscus movement of the gas-liquid interface in *U-model* and *H-model*. The arrows indicate the direction of progress. During the invasion, the invading phase needs to overcome the entry capillary pressure (Mason & Morrow, 1994), which is calculated as:

$$P_c = \frac{\gamma}{r_c} = \frac{\gamma \cos(180° - \theta - \alpha)}{\frac{1}{2}d + R[1 - \cos(\alpha)]} \tag{3}$$

Here, α and θ are the filling angle and contact angle. α varies from $-90°$ to $90°$ during displacement process. γ is the surface tension. d is the gap between the cylinders, that is, d_1 and d_2 for 1st-order structure and 2nd-order structure. Finally, R is the cylinder radius, that is, R_1 and R_2 for uniform and hierarchical structures.

As an example of gas replacement by liquid, Figure 7a shows the complete process of meniscus advancement in the range of the filling angle $\alpha \in (-90°, 90°)$. Local wettability on the interface of the cylinder is assumed to be constant, which means that the angle between the meniscus and the cylindrical surface keeps at $180° - 75° = 105°$ in each position. Figure 7b illustrates the evolution of meniscus curvature radius r_c as increase of α. Different order structures have various r_c due to different the gap between neighboring cylinders d. According to Equation 3, P_c is equal to zero when α equal to critical filling angle $\alpha_0 = 90° - \theta = -15°$. As shown in Figure 7c, the general pore infiltration process can be divided into two parts based on the value of α_0.

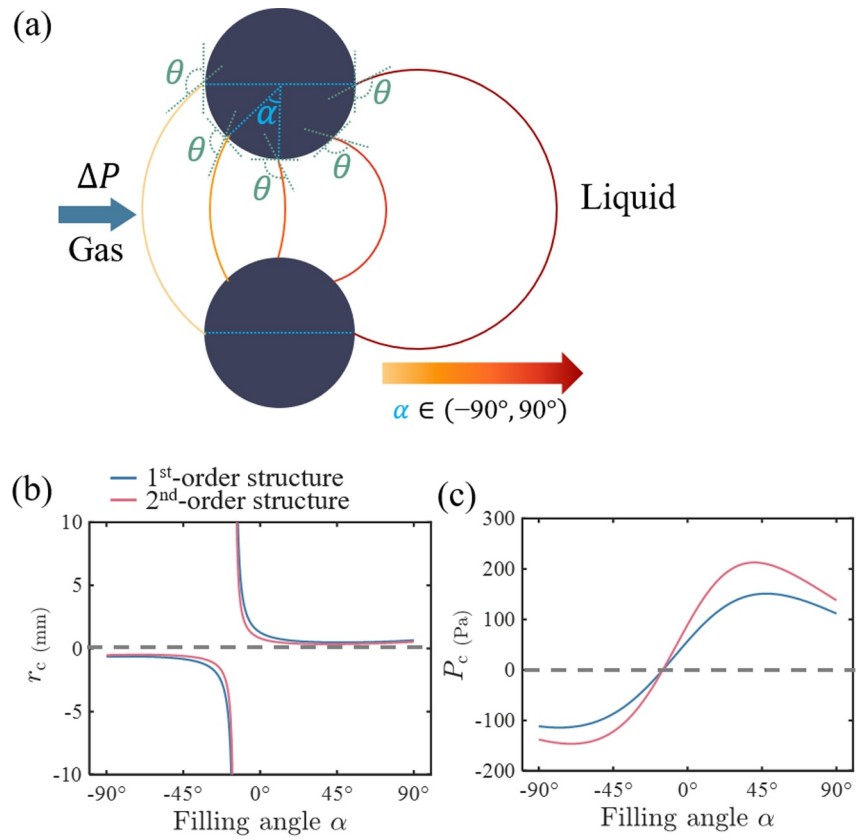

Figure 7. Schematic diagram of meniscus advancement process in the range of the filling angle $\alpha \in (-90°, 90°)$ during gas displacement of liquid. (b) Curves of filling angle α versus curvature radius r_c at different order structures. (c) Curves of filling angle α versus entry capillary pressure P_c in Equation 3 at different order structures.

When $\alpha < \alpha_0$, P_c is negative and spontaneous process occurs, which means the meniscus moves spontaneously. When $\alpha > \alpha_0$, P_c is positive and inhibited process occurs, which means an external driving force needs to be provided to the meniscus to infiltrate the 2nd-order pore. As shown in Figure 7c, while 2nd-order structure has a stronger negative capillary force to imbibe the meniscus into the pore compared to 1st-order structure, it also requires a stronger external driving force to overcome the stronger positive entry capillary force once it exceeds the critical filling angle.

Clearly, the narrower gap d_2 in the 2nd-order structure compared to the 1st-order structure is the reason for stronger P_c. The higher entry capillary pressure suggests an increased energy barrier, enhancing the stability of the menisci. It can be used to explain the main findings in Section 3.1, regarding the preferential invasion in 1st-order structure and strong capillary trapping of 2nd-order structure. In addition, the discrete-domain model also can be employed to elucidate the weaker saturation hysteresis effect in *H-model* mentioned earlier. The inhibition of menisci motion in *H-model* indicates a relatively stable gas-liquid distribution during cycle injection. Therefore, the saturation hysteresis effect is limited in *H-model*.

During the invading process, not only the invading phase mobilized, but also the defending phase mobilized forward. As shown in *U-model* of Figures S6a, S6c, and S6e in Supporting Information S1, the newly invaded liquid (light blue) in gas invasion and the newly invaded gas (light red) in liquid invasion indicate the mobilization of residual ganglion, which are obtained by the area increment of the defending phase after the invasion. As shown in Figure S6 in Supporting Information S1, the mobilization of ganglion weakens as the decrease of invasion speed. The movement of the defending phase is caused by the pushing of the invading phase. At a lower flow rate, the capillary number *Ca* reduces, which enhances the influence of interfacial tension forces. Therefore, it is easy for the invading phase to be trapped in porous structures. Compared with *U-model*, the mobilization of

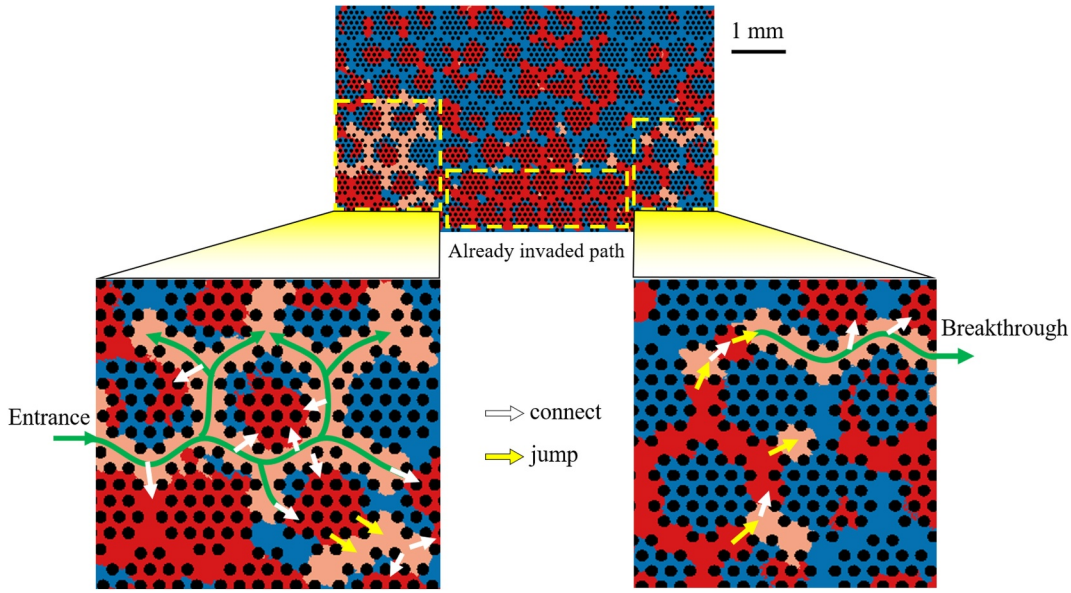

Figure 8. Connect-jump invasion method in cycle 2 of hierarchical porous structure at a flow rate of 170 mL/hr.

residual ganglion is rarely observed in *H-model* at all flow rates (Figures S6b, S6d, and S6f in Supporting Information S1).

In order to explain the inhibited mobilization of the ganglion in *H-model*, gas invasion in cycle 2 of *H-model* at a flow rate of 170 mL/hr is taken as an example to explore the local invasion behavior in Figure 8. As shown in the green curved arrow, gas enters porous media from the inlet and mainly invades in 1st-order structure. During the progress, the gas consistently connects with the residual trapped gas in 2nd-order cells as shown in white arrows. Even though the 1st-order path around the 2nd-order cell is displaced by gas, there is still liquid remaining in the 2nd-order cell. When gas connects to the residual gas in a cell in front of it, the gas invasion will jump directly to the front side of the residual gas, as shown by the yellow arrows. If there is already an invaded gas path ahead, gas will reduce the invasion time, quickly approach the outlet, and breakthrough. This invasion method means that the newly invading phase does not form a completely new invading path to breakthrough. The early breakthrough allows the gas to release the local energy barrier P_c, which causes the decrease of pressure difference. Therefore, the smaller newly invaded area (light red) in Figure S6 in Supporting Information S1 is observed. This is the reason why the approaching of zero hysteresis in Figure 5a. The connect-jump invasion method also occurs during the liquid invasion. The mechanism of ganglion mobilization suppression can be explained by the connect-jump invasion method. Due to lower entry capillary pressure P_c, it becomes easier for the invading phase to invade in the 1st-order structure. It merely goes around the 2nd-order structure and connects the residual phases inside. Therefore, the threshold capillary pressure of the 2nd-order structure for ganglion movement to occur was not achieved. In addition, the defending phase rarely existed in isolation in 1st-order structure. Most of them were connected to the defending phases in the 2nd-order structure. Therefore, the residual ganglion movement is reduced in the hierarchical structure.

3.4. Topology Connectivity and Permeability

To investigate the mechanism of hysteresis difference between uniform and hierarchical structure, the fluid connectivity in porous media was characterized by a topological invariant, that is, Euler number (or Euler characteristic) χ (Herring et al., 2013; Wildenschild & Sheppard, 2013). It provides a structure characterization of a topological object that remains unchanged even under deformation, which can be calculated from the family of Betti numbers:

$$\chi = \beta_0 - \beta_1 + \beta_2. \quad (4)$$

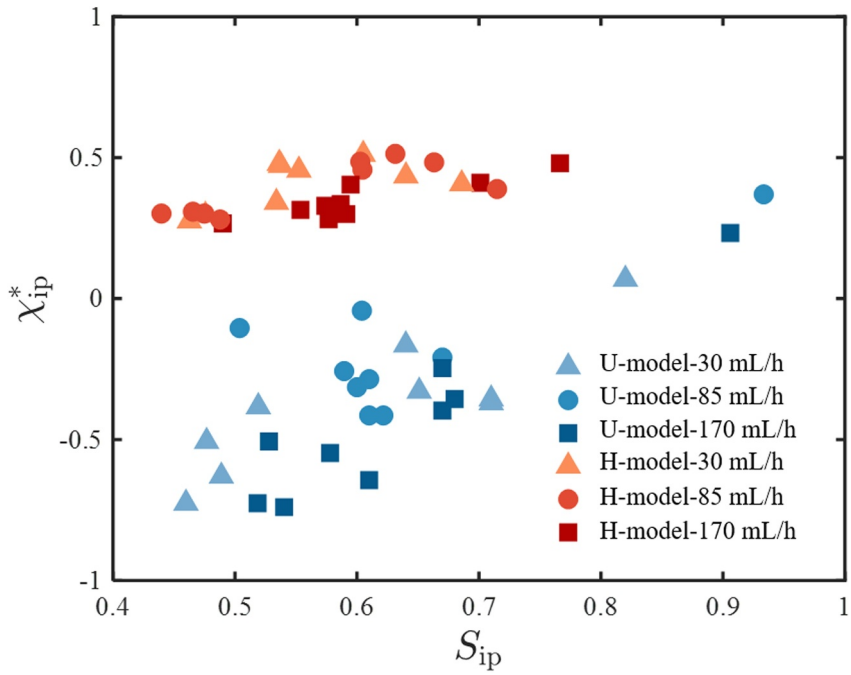

Figure 9. Normalized Euler number χ^*_{ip} versus saturation S_{ip} in uniform and hierarchical structures ("ip" represents the invading phase).

For a three-dimensional object, the zeroth Betti number β_0 corresponds to the number of disconnected fluid elements, the first Betti number β_1 represents the number of "handles" or loops within the structure of each fluid element, and the second Betti number β_2 signifies the number of isolated voids or cavities in the fluid elements. Notably, in our two-dimensional model, the value of β_2 is equal to 0. The calculation of the Euler number was performed using a self-developed MATLAB code. "bweuler" function was mainly used to measure Betti numbers and calculate the Euler number. It should be noted that the calculation here pertains to the topological connectivity of the pore space (or the fluid occupying that space), rather than the connectivity of the solid phase. Before the first water invasion, the porous structure is initially saturated with gas. In this condition, β_0 is equal to 1 and the β_1 is equal to the number of cylinders in the porous domain (74 for *U-model* and 2,324 for *H-model*). Therefore, the initial Euler numbers χ_0 for *U-model* and *H-model* differ significantly, being -73 and $-2{,}323$, respectively. For reasonable comparisons across various porous media, the normalized Euler number χ^* was introduced, which is defined as the ratio of the Euler number of phases χ to the initial Euler number χ_0, that is, $\chi^* = \chi/\chi_0$. The negative initial Euler number χ_0 will change the sign. Therefore, the closer to 1 the normalized Euler number χ^* is, the higher connectivity the phase has. A negative normalized Euler number indicates the presence of numerous disconnected ganglia.

Figure 9 shows the normalized Euler number χ^*_{ip} of invading phase as a function of saturation S_{ip} during the cyclic water-gas invasion with different invasion speeds. The normalized Euler number exhibits a slowly upward trend with increasing saturation. As mentioned above, Euler number is a topological invariant that ignores deformation. Although increasing the phase area does not directly lead to an increase in normalized Euler number, it does have the potential to influence the interconnection between the fluids. As shown in Figure 9, the normalized Euler number of *U-model* is lower than 0, except for three data points, which are from the first water invasion at cycle 0. The water almost fills the entire porous structure, so the topological connectivity is quite high. However, the *H-model* keeps the positive normalized Euler number, fluctuating between 0.2 and 0.5 throughout the cyclic injection for all invasion flow rates. This demonstrates that, during cycle invasion, the invading phase shows significantly higher connectivity in *H-model* compared to *U-model*. The extra void spaces within the 2nd-order structure are the primary factor contributing to higher connectivity of *H-model*. The weaker hysteresis effect observed in *H-model* can be attributed to their high connectivity, as discussed earlier. The high phase connectivity in porous media signifies the presence of established invasion pathways, facilitating breakthrough events. Rapid

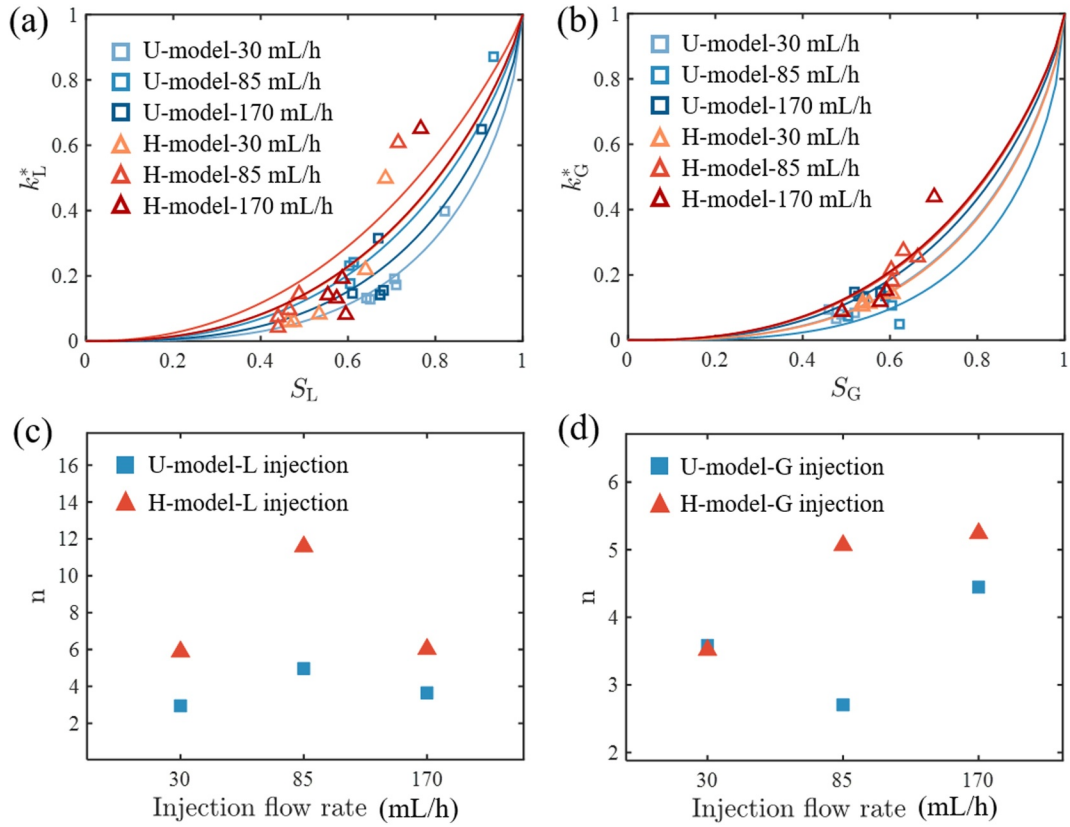

Figure 10. (a, b) Relative permeability versus saturation for liquid and gas invasions, respectively (solid lines is the van Genuchten model fitting curve (Van Genuchten, 1980)) and (c, d) comparison of van Genuchten parameter between *U-model* and *H-model* for liquid and gas injection, respectively.

breakthrough can alleviate entry capillary pressure, which means gas does not need to cross the local energy barrier to connect the outlet. The reduced pressure difference constrains the movement of the meniscus, thereby stabilizing the saturation distribution in the porous domain. Therefore, the hysteresis effect is restricted in the hierarchical structure.

Relative permeability is a characteristic of the invading phase conductivity, reflecting the ease with which the invading phase flows through the porous media. The phase permeability k is calculated based on the obtained images using LBM simulation (see Figure S4 in Supporting Information S1). Then, the relative permeability k^* of the invading phase at each invasion was calculated:

$$k^* = \frac{k}{k_{\text{abs,max}}} \tag{5}$$

Here, the initial maximum absolute permeability $k_{\text{abs,max}}$ is obtained when the porous media is 100% saturated with a single phase. For *U-model* and *H-model*, $k_{\text{abs,max}}$ is 0.5 and 2.9 m^2, respectively. As illustrated by Figures 10a and 10b, the relative permeability k^* shows a positive relationship with the saturation S for liquid and gas invasions. To compare the difference between *U-model* and *H-model*, the van Genuchten model analytically integrated into the Mualem's relative permeability model (Mualem, 1976; Van Genuchten, 1980) was used to fit the data:

$$k^* = S^{\epsilon}\left(1 - \left(1 - S^{1/m}\right)^m\right)^2 \tag{6}$$

Here, ϵ is related to the connection between pores and invading channel tortuosity. According to (Sheng et al., 2019), ϵ is equal to zero. $m = 1 - 1/n$ is a van Genuchten parameter, related to the symmetry of liquid retention curves. Since the van Genuchten model is applicable at the continuum scale, the chosen zone of interest must serve as a representative volume element (RVE) (Bruchon et al., 2013). In this study, the porous domain on the chip consists of 12 2nd-order cells in the invasion direction and 9 in the perpendicular direction, which is the maximum within the constraints of the 3D printer's maximum size and resolution. Given the importance of the invasion direction, the number of 2nd-order cells in this direction is close to 14 2nd-order cells used in the simulation study on hierarchical structure by Suo et al. (2020). Additionally, we measured the saturation profile within various volume element widths along with the injection direction. More detailed description can be found in Figure S8 in Supporting Information S1. The results of *H-model* and *U-model* both demonstrate that saturation fluctuates within smaller volume elements and before the volume element width reaches a maximum value (i.e., equal to the entire width of the porous medium) the saturation becomes stable as the volume element width increases. Accordingly, our selected zone of interest in *H-model* and *U-model* is suitable to be considered as a RVE. Naturally, caution must be exercised when extrapolating the current permeability findings to hierarchical structures larger than the RVE. After fitting the data by using this model, n was estimated and plotted in Figures 10c and 10d. It was found that n of *H-model* is much higher than that of *U-model*. A larger n indicates that the fitted curve is closer to the diagonal in Figures 10a and 10b, meaning the invading phase has a higher permeability at the same saturation level. The main reason for the higher n value in *H-model* is the arrangement of pores. The space in each 2nd-order cell in the hierarchical structure provides more invadable channels for the invading phase compared to the uniform structure, potentially increasing relative permeability. However, Figures 10a and 10b show that the relative permeability of the *H-model* surpasses the *U-model* only at high saturation. The mechanism behind this needs to be further parametric exploration by experiments.

4. Conclusions

This study investigates the hysteretic behaviors of alternating gas-liquid injection cycles in hierarchical porous media. The findings reveal that the hierarchical structure, featuring both 1st-order and 2nd-order pores, exhibits distinct fluid displacement characteristics compared to the uniform structure only with 1st-order pores. The preferential invasion and stronger capillary trapping in the 1st-order and 2nd-order structures, respectively, along with the suppression of residual ganglion mobilization in the hierarchical structure, highlight the impact of pore hierarchy on fluid behavior. Additionally, the hierarchical structure demonstrates the weaker hysteresis effect, attributed to the higher entry capillary pressure in the 2nd-order structure and better topological connectivity. Permeability estimations using the van Genuchten model further indicate that the hierarchical media has a larger van Genuchten parameter due to the additional pore space in 2nd-order structure.

These findings contribute to optimization of the storage and extraction strategies in UHS, in particular to consider the hysteretic behavior when rock heterogeneity contains distinct characteristic pore sizes. For example, this hierarchical structure demonstrates greater topological connectivity and permeability, which helps minimize the occurrence of disconnected hydrogen ganglia, potentially reducing hydrogen losses. However, the most significant finding of this study is that the hierarchical heterogeneous structure has a weaker hysteresis effect, which will lead to a decrease in hydrogen storage and withdrawal efficiency. Thus, if the subsurface rock structure at the target storage site is modeled as the homogeneous structure to assess storage and extraction capacity, significant errors may arise.

The discrepancies between hierarchical and uniform porous structures demonstrated in this paper warrant further research updating the current understanding on homogeneous media for subsurface resource applications. For example, the huge contrast between different levels of pore sizes in the hierarchical structure implies a stronger effect of wettability, which needs to be further investigated. The current conclusions are based on cases with three injection flow rates, all within the capillary fingering regime. Therefore, future studies with higher injection flow rates are necessary to extend these conclusions to the viscous fingering regime. Additionally, our current study is limited to 2D models due to the difficulty of fabrication and fluid imaging. The addition of third dimensional orientation may increase the available space for fluid invasion, potentially enhancing permeability. This increase in dimension may result in a more significant hysteresis difference between 3D homogeneous and hierarchical structures. In the future, we are looking forward to extending 2D hierarchical model to 3D.

Data Availability Statement

Details of experiments and the images can be found in Supporting Information S1, and the data sets associated with this work are available at S. Yang et al. (2025).

Acknowledgments
The authors thank Cornelius Wittig and Wenhai Lei in Fluid and Surfaces Group of KTH for their help with the 3D printing and useful discussions on chip design and reproducibility. Besides, the authors also want to thank Danan Yang in Lund University and Haiyi Zhong in The University of Sydney for helpful discussions on representative volume element (RVE).

References

Ahn, H., Kim, S.-O., Lee, M., & Wang, S. (2020). Migration and residual trapping of immiscible fluids during cyclic injection: Pore-scale observation and quantitative analysis. *Geofluids*, *2020*(1), 4569208. https://doi.org/10.1155/2020/4569208

Bakhshian, S., & Sahimi, M. (2017). Adsorption-induced swelling of porous media. *International Journal of Greenhouse Gas Control*, *57*, 1–13. https://doi.org/10.1016/j.ijggc.2016.12.011

Broers, H. P., Sültenfuß, J., Aeschbach, W., Kersting, A., Menkovich, A., de Weert, J., & Castelijns, J. (2021). Paleoclimate signals and groundwater age distributions from 39 public water works in The Netherlands; insights from noble gases and carbon, hydrogen and oxygen isotope tracers. *Water Resources Research*, *57*(7), e2020WR029058. https://doi.org/10.1029/2020WR029058

Bruchon, J.-F., Pereira, J.-M., Vandamme, M., Lenoir, N., Delage, P., & Bornert, M. (2013). X-ray microtomography characterisation of the changes in statistical homogeneity of an unsaturated sand during imbibition. *Géotechnique Letters*, *3*(2), 84–88. https://doi.org/10.1680/geolett.13.00013

Carlson, F. M. (1981). Simulation of relative permeability hysteresis to the nonwetting phase. In *Paper presented at SPE annual technical conference and exhibition?* SPE. https://doi.org/10.2118/10157-MS

Celia, M. A., Bachu, S., Nordbotten, J. M., & Bandilla, K. W. (2015). Status of CO_2 storage in deep saline aquifers with emphasis on modeling approaches and practical simulations. *Water Resources Research*, *51*(9), 6846–6892. https://doi.org/10.1002/2015WR017609

Cueto-Felgueroso, L., & Juanes, R. (2016). A discrete-domain description of multiphase flow in porous media: Rugged energy landscapes and the origin of hysteresis. *Geophysical Research Letters*, *43*(4), 1615–1622. https://doi.org/10.1002/2015GL067015

Das, D., & Nassehi, V. (2003). Modeling of contaminants mobility in underground domains with multiple free/porous interfaces. *Water Resources Research*, *39*(3), 1072. https://doi.org/10.1029/2002WR001506

Datta, S. S., & Weitz, D. A. (2013). Drainage in a model stratified porous medium. *EPL*, *101*(1), 14002. https://doi.org/10.1209/0295-5075/101/14002

Edlmann, K., Hinchliffe, S., Heinemann, N., Johnson, G., Ennis-King, J., & McDermott, C. (2019). Cyclic CO_2–H_2O injection and residual trapping: Implications for CO_2 injection efficiency and storage security. *International Journal of Greenhouse Gas Control*, *80*, 1–9. https://doi.org/10.1016/j.ijggc.2018.11.009

Gu, Q., Liu, H., & Wu, L. (2021). Preferential imbibition in a dual-permeability pore network. *Journal of Fluid Mechanics*, *915*, A138. https://doi.org/10.1017/jfm.2021.174

Hematpur, H., Abdollahi, R., Rostami, S., Haghighi, M., & Blunt, M. (2023). Review of underground hydrogen storage: Concepts and challenges. *Advances in Geo-Energy Research*, *7*(2), 111–131. https://doi.org/10.46690/ager.2023.02.05

Herring, A. L., Sun, C., Armstrong, R., Li, Z., McClure, J., & Saadatfar, M. (2021). Evolution of bentheimer sandstone wettability during cyclic $scCO_2$-brine injections. *Water Resources Research*, *57*(11), e2021WR030891. https://doi.org/10.1029/2021WR030891

Herring, A. L., Harper, E. J., Andersson, L., Sheppard, A., Bay, B. K., & Wildenschild, D. (2013). Effect of fluid topology on residual nonwetting phase trapping: Implications for geologic CO_2 sequestration. *Advances in Water Resources*, *62*, 47–58. https://doi.org/10.1016/j.advwatres.2013.09.015

Hu, R., Lan, T., Wei, G.-J., & Chen, Y.-F. (2019). Phase diagram of quasi-static immiscible displacement in disordered porous media. *Journal of Fluid Mechanics*, *875*, 448–475. https://doi.org/10.1017/jfm.2019.504

Jerauld, G. (1997). General three-phase relative permeability model for Prudhoe Bay. *SPE Reservoir Engineering*, *12*(04), 255–263. https://doi.org/10.2118/36178-PA

Kang, J., & Wang, M. (2024). Brinkman double-layer model for flow at a free-porous interface. *International Journal of Mechanical Sciences*, *263*, 108770. https://doi.org/10.1016/j.ijmecsci.2023.108770

Korson, L., Drost-Hansen, W., & Millero, F. J. (1969). Viscosity of water at various temperatures. *The Journal of Physical Chemistry*, *73*(1), 34–39. https://doi.org/10.1021/j100721a006

Land, C. S. (1968). Calculation of imbibition relative permeability for two-and three-phase flow from rock properties. *Society of Petroleum Engineers Journal*, *8*(02), 149–156. https://doi.org/10.2118/1942-PA

Lei, W., Gong, W., Lu, X., & Wang, M. (2024). Fluid entrapment during forced imbibition in a multidepth microfluidic chip with complex porous geometry. *Journal of Fluid Mechanics*, *987*, A3. https://doi.org/10.1017/jfm.2024.358

Lei, W., Lu, X., Gong, W., & Wang, M. (2023). Triggering interfacial instabilities during forced imbibition by adjusting the aspect ratio in depth-variable microfluidic porous media. *Proceedings of the National Academy of Sciences of the United States of America*, *120*(50), e2310584120. https://doi.org/10.1073/pnas.2310584120

Liu, H., Valocchi, A. J., Werth, C., Kang, Q., & Oostrom, M. (2014). Pore-scale simulation of liquid CO_2 displacement of water using a two-phase lattice Boltzmann model. *Advances in Water Resources*, *73*, 144–158. https://doi.org/10.1016/j.advwatres.2014.07.010

Lu, N. B., Browne, C. A., Amchin, D. B., Nunes, J. K., & Datta, S. S. (2019). Controlling capillary fingering using pore size gradients in disordered media. *Physical Review Fluids*, *4*(8), 084303. https://doi.org/10.1103/PhysRevFluids.4.084303

Lysyy, M., Føyen, T., Johannesen, E. B., Fernø, M., & Ersland, G. (2022). Hydrogen relative permeability hysteresis in underground storage. *Geophysical Research Letters*, *49*(17), e2022GL100364. https://doi.org/10.1029/2022GL100364

Lysyy, M., Liu, N., Solstad, C. M., Fernø, M. A., & Ersland, G. (2023). Microfluidic hydrogen storage capacity and residual trapping during cyclic injections: Implications for underground storage. *International Journal of Hydrogen Energy*, *48*(80), 31294–31304. https://doi.org/10.1016/j.ijhydene.2023.04.253

Mason, G., & Morrow, N. R. (1994). Effect of contact angle on capillary displacement curvatures in pore throats formed by spheres. *Journal of Colloid and Interface Science*, *168*(1), 130–141. https://doi.org/10.1006/jcis.1994.1402

Mualem, Y. (1976). A new model for predicting the hydraulic conductivity of unsaturated porous media. *Water Resources Research*, *12*(3), 513–522. https://doi.org/10.1029/WR012i003p00513

Nijjer, J. S., Hewitt, D. R., & Neufeld, J. A. (2019). Stable and unstable miscible displacements in layered porous media. *Journal of Fluid Mechanics*, *869*, 468–499. https://doi.org/10.1017/jfm.2019.190

Porter, M. L., Wildenschild, D., Grant, G., & Gerhard, J. I. (2010). Measurement and prediction of the relationship between capillary pressure, saturation, and interfacial area in a NAPL-water-glass bead system. *Water Resources Research*, *46*(8), W08512. https://doi.org/10.1029/2009WR007786

Rabbani, H. S., Or, D., Liu, Y., Lai, C.-Y., Lu, N. B., Datta, S. S., et al. (2018). Suppressing viscous fingering in structured porous media. *Proceedings of the National Academy of Sciences of the United States of America*, *115*(19), 4833–4838. https://doi.org/10.1073/pnas.1800729115

Rezaei, A., Hassanpouryouzband, A., Molnar, I., Derikvand, Z., Haszeldine, R. S., & Edlmann, K. (2022). Relative permeability of hydrogen and aqueous brines in sandstones and carbonates at reservoir conditions. *Geophysical Research Letters*, *49*(12), e2022GL099433. https://doi.org/10.1029/2022GL099433

Seibt, D., Vogel, E., Bich, E., Buttig, D., & Hassel, E. (2006). Viscosity measurements on nitrogen. *Journal of Chemical Engineering Data*, *51*(2), 526–533. https://doi.org/10.1021/je050399c

Sheng, J., Huang, T., Ye, Z., Hu, B., Liu, Y., & Fan, Q. (2019). Evaluation of van Genuchten-Mualem model on the relative permeability for unsaturated flow in aperture-based fractures. *Journal of Hydrology*, *576*, 315–324. https://doi.org/10.1016/j.jhydrol.2019.06.047

Spiteri, E. J., Juanes, R., Blunt, M. J., & Orr, F. M. (2008). A new model of trapping and relative permeability hysteresis for all wettability characteristics. *SPE Journal*, *13*(03), 277–288. https://doi.org/10.2118/96448-PA

Suo, S., & Gan, Y. (2021). Tuning capillary flow in porous media with hierarchical structures. *Physics of Fluids*, *33*(3), 034107. https://doi.org/10.1063/5.0038634

Suo, S., Liu, M., & Gan, Y. (2020). Fingering patterns in hierarchical porous media. *Physical Review Fluids*, *5*(3), 034301. https://doi.org/10.1103/PhysRevFluids.5.034301

Tanaka, M., Girard, G., Davis, R., Peuto, A., & Bignell, N. (2001). Recommended table for the density of water between 0 C and 40 C based on recent experimental reports. *Metrologia*, *38*(4), 301–309. https://doi.org/10.1088/0026-1394/38/4/3

Tarkowski, R. (2019). Underground hydrogen storage: Characteristics and prospects. *Renewable and Sustainable Energy Reviews*, *105*, 86–94. https://doi.org/10.1016/j.rser.2019.01.051

Van Genuchten, M. T. (1980). A closed-form equation for predicting the hydraulic conductivity of unsaturated soils. *Soil Science Society of America Journal*, *44*(5), 892–898. https://doi.org/10.2136/sssaj1980.03615995004400050002x

Vargaftik, N., Volkov, B., & Voljak, L. (1983). International tables of the surface tension of water. *Journal of Physical and Chemical Reference Data*, *12*(3), 817–820. https://doi.org/10.1063/1.555688

Wang, Z., Chauhan, K., Pereira, J.-M., & Gan, Y. (2019). Disorder characterization of porous media and its effect on fluid displacement. *Physical Review Fluids*, *4*(3), 034305. https://doi.org/10.1103/PhysRevFluids.4.034305

Wang, Z., Pereira, J.-M., Sauret, E., & Gan, Y. (2023). Wettability impacts residual trapping of immiscible fluids during cyclic injection. *Journal of Fluid Mechanics*, *961*, A19. https://doi.org/10.1017/jfm.2023.222

Wildenschild, D., & Sheppard, A. P. (2013). X-ray imaging and analysis techniques for quantifying pore-scale structure and processes in subsurface porous medium systems. *Advances in Water Resources*, *51*, 217–246. https://doi.org/10.1016/j.advwatres.2012.07.018

Wolf, F. G., Siebert, D. N., Carreño, M. N., Lopes, A. T., Zabot, A. M., & Surmas, R. (2022). Dual-porosity micromodels for studying multiphase fluid flow in carbonate rocks. *Lab on a Chip*, *22*(23), 4680–4692. https://doi.org/10.1039/D2LC00445C

Yang, D., Andersson, M., & Garg, H. (2024). Effect of fiber curvature on gas diffusion layer two-phase dynamics of proton exchange membrane fuel cells. *International Journal of Hydrogen Energy*, *85*, 635–651. https://doi.org/10.1016/j.ijhydene.2024.08.307

Yang, S., Kong, G., Cao, Z., Wu, Z., & Li, H. (2022). Hydrodynamics of gas-liquid displacement in porous media: Fingering pattern evolution at the breakthrough moment and the stable state. *Advances in Water Resources*, *170*, 104324. https://doi.org/10.1016/j.advwatres.2022.104324

Yang, S., Kong, G., & Wu, Z. (2021). Experimental study of gas-liquid mass transfer in a rectangular microchannel by digital image analysis method. In *Paper presented at ASME international mechanical engineering congress and exposition*. American Society of Mechanical Engineers. https://doi.org/10.1115/IMECE2021-69095

Yang, S., Li, H., Suo, S., & Wu, Z. (2024). Viscous-dependent fingering dynamics of gas invading into multi-fluids. *Advances in Water Resources*, *191*, 104757. https://doi.org/10.1016/j.advwatres.2024.104757

Yang, S., Suo, S., Gan, Y., Bagheri, S., Wang, L., & Revstedt, J. (2025). Experimental study on hysteresis during cyclic injection in hierarchical porous media [Dataset]. *Figshare*. https://doi.org/10.6084/m9.figshare.28152137

Zhang, C., Oostrom, M., Grate, J. W., Wietsma, T. W., & Warner, M. G. (2011). Liquid CO_2 displacement of water in a dual-permeability pore network micromodel. *Environmental Science & Technology*, *45*(17), 7581–7588. https://doi.org/10.1021/es201858r

Zhong, H., Wang, Z., Zhang, Y., Suo, S., Hong, Y., Wang, L., & Gan, Y. (2024). Gas storage in geological formations: A comparative review on carbon dioxide and hydrogen storage. *Materials Today Sustainability*, *26*, 100720. https://doi.org/10.1016/j.mtsust.2024.100720